

# Bioinspired Controllable Electro-Chemomechanical Coloration Films

Yinhua Bao, Yu Han, Le Yang, Na Li, Jingdong Luo, Wenjie Qu, Renjie Chen, Alex K.-Y. Jen, Teng Li, Haosen Chen,\* Wei-Li Song,\* and Daining Fang\*

Coloration materials and devices with broad manipulatable color spectra and precisely controllable capability are highly pursued in various applications, such as camouflage engineering, optical sensors, anticounterfeiting technology, real-time monitoring, and so on. For achieving the goals, in the present work, a conceptually novel bioinspired coloration film is demonstrated using nanoscale amorphous silicon (a-Si) layer deposited on a reflective metal substrate. With precisely manipulating the reversible lithiation/delithiation behaviors, such coloration films enable to present consecutively tunable chromogenic property in a broad visible band, since the simultaneous changes in both chemical components and film thickness upon electrochemical processes substantially vary the conditions of destructive interference. Accordingly, the corresponding model based on electro-chemomechanical coupling effects confirms the coloration mechanism induced by thickness and intrinsic properties (refraction index and optical absorptivity). Additionally, such coloration films also suggest universal design ability, namely tailoring the coloration spectra via simply changing film thicknesses and metal substrates. Thus, the results promise a versatile strategy for fabricating advanced coloration materials and devices that are pursued in specular reflection, sensing, anticounterfeiting, labels, displaying, and sensors.

reflection from their tunable epidermis structures. For instance, cephalopods, such as cuttlefish and squids, can change their body coloration by manipulating their iridophores within their mantle. The dynamic light reflection produced by the iridophores can be attributed to the reversible change of the platelet thickness and the overall effective refractive index of the platelet stacks within the iridophores.<sup>[1]</sup> Besides, some squids (e.g., *Lolliguncula brevis*) can also provide a unique function for active cells changing its color from iridescent to noniridescent through the gel–sol transitional mode of proteinaceous material within the iridophore platelets in their dermis.<sup>[2]</sup> Some insects such as the *Hercules beetles* and *tortoise beetles* can change the color of their elytra under different ambient humidity. The mixed layered structures underneath their skins contribute to the alternative interference colors by absorbing or exuding the water molecules in the cuticle.<sup>[3,4]</sup> Inspired by these natural creatures, artificial

color structural materials upon the external stimuli such as electrical field,<sup>[5–7]</sup> humidity,<sup>[8]</sup> mechanical force,<sup>[9]</sup> and concentration of specific molecules were highly pursued for application in sensors, optical filters, anticounterfeiting, and light-responsive/adaptive coating.<sup>[10]</sup>

## 1. Introduction

Most biological systems display astonishing structural colors for camouflage, signal communication, and thermoregulation in consequence of thin film interference, and selective

Y. Bao, L. Yang, Prof. D. Fang  
State Key Laboratory for Turbulence and Complex System  
College of Engineering  
Peking University  
Beijing 100871, China  
E-mail: fangdn@pku.edu.cn

Y. Bao, Prof. T. Li  
Department of Mechanical Engineering  
University of Maryland  
College Park, MD 20742, USA

Y. Han, N. Li, Prof. H. Chen, Prof. W.-L. Song, Prof. D. Fang  
Institute of Advanced Structure Technology  
Beijing Institute of Technology  
Beijing 100081, China  
E-mail: chenhs@bit.edu.cn; weilis@bit.edu.cn

Prof. J. Luo, Prof. A. K.-Y. Jen  
Department of Chemistry  
City University of Hong Kong  
Kowloon 999077, Hong Kong, China

Dr. W. Qu, Prof. R. Chen  
Beijing Key Laboratory of Environmental Science  
and Engineering  
School of Material Science and Engineering  
Beijing Institute of Technology  
Beijing 100081, P. R. China

Prof. A. K.-Y. Jen  
Department of Chemistry  
University of Washington  
Seattle, WA 98195, USA

 The ORCID identification number(s) for the author(s) of this article can be found under <https://doi.org/10.1002/adfm.201806383>.

DOI: 10.1002/adfm.201806383

Bioinspired color materials, based on interference, reflection and antireflection, have been previously studied to achieve a multiple color display.<sup>[11–13]</sup> As one of the bioinspired color materials, silicon-based materials can be readily designed as various nanostructures such as multilayer stacks,<sup>[14]</sup> origami,<sup>[15]</sup> nanowire,<sup>[16]</sup> and nanotips.<sup>[17]</sup> By controlling their scales, structures, (e.g., layer thickness) and variability of their refractive indices, these silicon optical nanostructures can be precisely arranged for diverse optical functions.<sup>[18,19]</sup> However, most silicon-based color structures are pre-designed, static and lacking stimuli-responsiveness, and dynamic tunability. On the other hand, photonic gel materials, another biomimetic photonic structural material, also show brilliant colored reflection attributed to thin film interference and diffraction.<sup>[20,21]</sup> The large volumetric change of the polymer soft matrix provides a tunable coloration in response to external stimuli like humidity,<sup>[8,22]</sup> mechanical force,<sup>[23,24]</sup> and temperature.<sup>[25]</sup> Some of the biomimetic polymer gels even exhibit the reversible color change through the entire range of the visible band, which are similar to the skin of a chameleon. However, the efficiency of photonic gels fabrication is limited, since most of them require a meticulously designed combination of multiple materials. In general, most bioinspired photonic structural materials designed on interference are focused on tunability in the chromatic range, and the switchable function from chromatic range to achromic range is still desired to integrate into those artificial photonic structures in a concise and controllable way.

Here, we developed a prototype of bioinspired controllable electro-chemomechanical coloration films based on simple physical structures via depositing a nanoscale amorphous silicon (a-Si) layer onto a reflective metal substrate. As an attractive electrode material in lithium ion battery, silicon anodes can present a large volume change upon insertion and extraction of lithium ions.<sup>[26–29]</sup> Analogizing with the volume change in photonic polymer gels, a silicon-based interference coloration film was fabricated by utilizing the atomic layer deposition technique. In contrast to commonly used biomimetic structural materials based on interference, the as-fabricated coloration films exhibit a consecutively controllable chromogenic property in a broad visible band. Moreover, it provides a unique switch capability between chromatic and achromic reflectance spectrums under the electro-chemomechanical control. A theoretical model combined with the systematic experimental results has been established to elucidate intrinsic mechanisms. During the chromatic stage, the thickness and overall effective refractive index of the coloration films are simultaneously changed by the lithiation/delithiation of a-Si. In addition, the transformation between chromatic stage and achromic stage is determined by the degree of alloying in a-Si nanofilm under voltage control. Furthermore, the effectiveness of the coloration design is demonstrated by manipulating the thickness of silicon nanofilms and categories of metal substrates, resulting in diverse coloration spectrums of films.

## 2. Results and Discussion

Analogizing with the neural control in the squids, the interference coloration film displays reversible colors under the

electro-chemomechanical control (**Figure 1a** and **Figure S1**, Supporting Information). It is placed horizontally to observe the reversible coloration during charge/discharge processes from the top views, while a Li counter electrode is placed around the interference coloration film in the electrochemical control cell to ensure uniform Li intercalation. **Figure 1b** shows the structure of the pristine interference coloration film. The film is sputtered on a silica glass substrate, which effectively stabilizes the film during Li intercalation and deintercalation processes (also see Supplementary methods in the Supporting information). A Cr layer is used to promote the adhesion among glass substrate, Cu layer, a-Si layer. The Cu layer serves as a current collector. Since the Cr layer between the Cu and a-Si layers is so thin that could be neglected for the optical characteristics of the entire film, it is not considered in the models for spectroscopic ellipsometry (SE) measurements and theoretical analysis. Besides the orange-red color of initial controllable coloration film, five representative colors, magenta, medium purple, dark blue, dark cyan, and gray (achromic) are clearly seen at different voltages during the Li intercalation process in **Figure 1c**.

The electro-chemomechanical mechanism is presented in **Figure 1d**. In the chromatic state, the nanoscaled a-Si film serves as an enhancement reflection coating while the copper film acts as a metalized film. One major reflected wave exists at the surface of the a-Si film, and another major reflected wave exists at the interface between the a-Si layer and the copper layer, which have different intensity at different wavelengths due to the selective absorption of the copper layer. These two reflected waves would have destructive interference because of the phase difference between them. Consequently, the reflectance spectrum of the coloration films is significantly decreased around the blue part of the visible band, leading to the observance of the orange-red color state. During the delithiated/lithiated cycling, the reversible chemical and physical evolutions are carried out simultaneously for the color tuning driven by the insertion/extraction of Li-ion. A-Si changes to  $\text{Li}_x\text{Si}$ , resulting in the variable optical component, index of refraction  $n$  and absorptivity  $k$  at different lithiation degrees. At the same time, the swelling/deswelling of Si nanoscaled film will contribute to the variable destructive interference in the nanoscale film structure at different lithiated states. Combining the two coupled evolutions in the film, the different colored state would be observed macroscopically and changed continuously by tuning the potential of the as-fabricated coloration films. Moreover, the contribution of the two evolutions to the color tuning could be adjustable by changing the lithiated degree. In the chromatic state, the physical evolution (thickness change of a-Si film) plays a leading role in the color tuning, causing the chromatic reflectance spectrum of the coloration films. When the film is under achromic state, the high absorptivity and large thickness of the  $\text{Li}_x\text{Si}$  film would weaken the destructive interference effects, and finally, show the achromic reflectance spectrum. To the best of our knowledge, this unique function would be significant to break through the chromatic color change limitation in most bioinspired photonic structural color systems designed based on interference.

To demonstrate the optical and electrochemical properties of the as-fabricated controllable coloration films thoroughly, a color change by charging and discharging was observed with

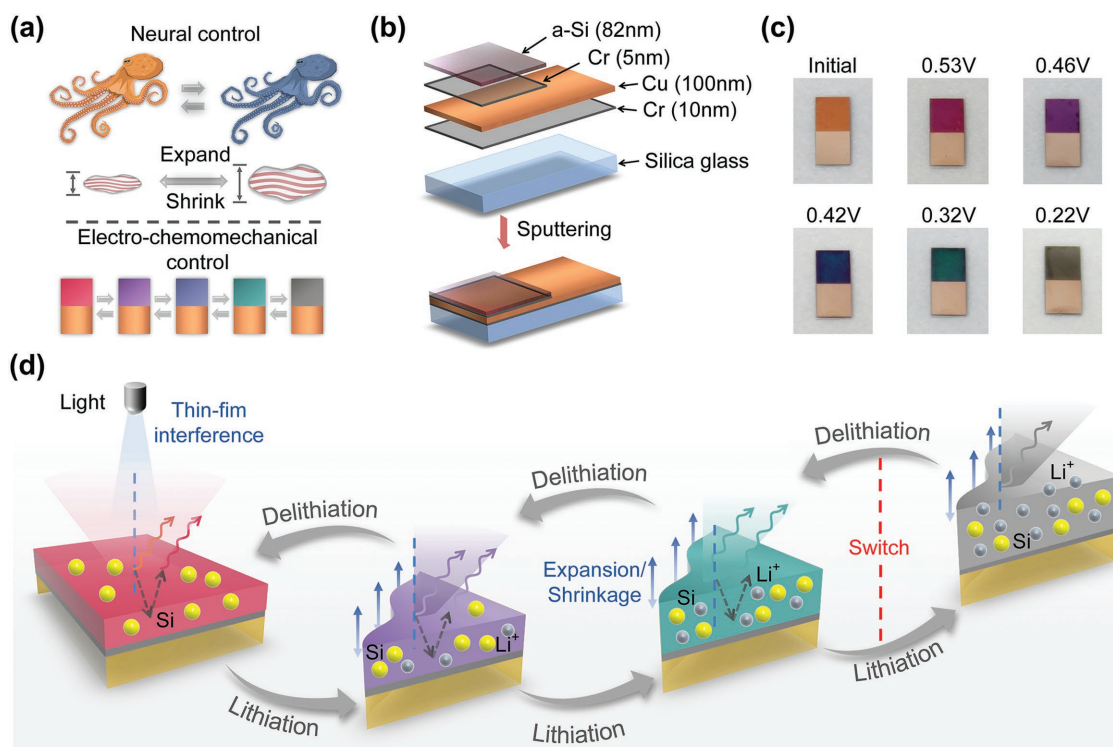


**Figure 1.** Fabrication and mechanism of the controllable interference coloration films. a) The reversible coloration process under electro-chemomechanical control inspired by the color change in the cephalopods by neutrally controlling the volume of cells or proteins. b) Schematic of the layered structure of the controllable coloration film. c) Photographs of controllable coloration films at different voltages during the Li intercalation process. The pictures are shot at discharge stage. The digital information of representative colors is shown in Table S1 (Supporting Information). d) Mechanisms of the chromatic and achromic process of the controllable coloration films.

a constant current density of  $4 \mu\text{A mm}^{-2}$  in the voltage range of 0.15–1.50 V. A charge/discharge profile of the coloration films during the first three cycles is illustrated in **Figure 2a**. The pristine orange-red color of the film only exists in the first discharge state, which is mainly due to the initial thickness increase of the a-Si film and the change of its optical properties. Because in this state, electrolyte components undergo sacrificial electrochemical decomposition and then form an ultrathin passivating solid electrolyte interphase (SEI) layer on the surface of film in the first cycle.<sup>[30]</sup> After that, the color change is highly reversible. In addition, the voltage ranges are consistent with its corresponding colors in the following cycles (Movie S1, Supporting Information).

To understand the correspondence between the color change and voltage quantitatively, the continuous color evolution is strictly divided into several parts (also see Supplementary methods in the Supporting Information). According to the time-related average HSL (hue, saturation, and lightness) color values of each recorded photograph in **Figure 2c**, the gray (achromic) state during coloration process is first defined by the range of saturation from 0 to 0.1. Apart from the color difference in the first discharge status, the reversible chromatic state is divided into four parts based on the standard hue partition in Munsell color wheel (**Figure 2d**), which are  $315^\circ$  to  $349^\circ$ ,  $261^\circ$  to  $315^\circ$ ,  $207^\circ$  to  $261^\circ$ ,  $153^\circ$  to  $207^\circ$ . Based on this, five reversible representative colors magenta, medium purple, dark blue, dark cyan, and gray (achromic) were picked up in

the inset of **Figure 2a**. Meanwhile, the corresponding voltage switch points are also marked at the profile of charge/discharge curve as blue circles, including red circles for dividing the first orange-red voltage range. Further, the estimated relationship between the representative colors and the  $\text{Li}^+$  content in coloration films is shown in **Figure S2** (Supporting Information). For each representative colors, the ranges of the corresponding  $\text{Li}^+$  content in the charge/discharge process are almost consistent, which demonstrates that the coloration process has a relationship with the  $\text{Li}^+$  content in coloration films and consequent thickness change of a-Si layer.

To evaluate the fast color change property of the controllable coloration films, the charge/discharge profiles of the films under the ultrahigh current density of  $40 \mu\text{A mm}^{-2}$  in well-chosen voltage range of 0.22–1.40 V are further illustrated in **Figure 2b**. Comparing the HSL values of each recorded photograph with charge/discharge profile data (**Figure S3**, Supporting Information), the whole color-switching period (magenta to gray, then back to magenta) is also strictly divided into five representative color parts. Surprisingly, the whole color-switching time dramatically decreases to 190 s while the chromatic and achromic functions are both well reserved and integrated. Meanwhile, as can be seen in **Figure S4** (Supporting Information), each representative color period could be reduced in seconds (e.g., achromic period 21 s), and the color-switching time between two close representative colors is fast with few seconds. For each charge/discharge cycle, the representative

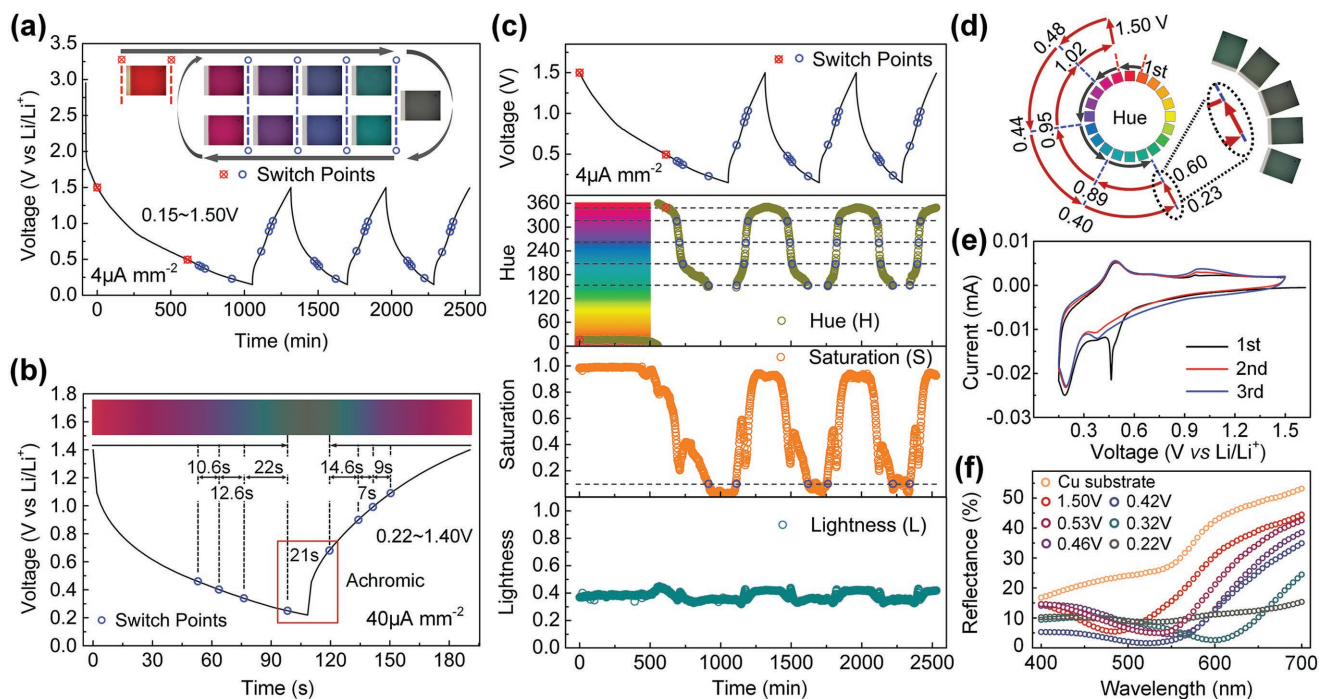


**Figure 2.** Optical and electrochemical characteristics of the controllable coloration films during the lithium ion insertion/extraction process. a) Charge/discharge profiles for the coloration films at a current density of  $4 \mu\text{A mm}^{-2}$  in the voltage range of 0.15–1.50 V, with the inset showing the microscopic views and color evolution at different charge/discharge voltages. b) Charge/discharge profiles for the coloration films at an ultra-high current density of  $40 \mu\text{A mm}^{-2}$  in the well-chosen voltage range of 0.22–1.40 V. c) The quantitative relationship between colors evolution (HSL values) and voltage under a current density of  $4 \mu\text{A mm}^{-2}$ . The blue and red circles marked in the voltage profile show the switch points of different colors parts. d) The division of colors evolution (hue) according to the standard Munsell color wheel, with the corresponding voltage at the switch points. e) Cyclic voltammograms of the coloration films in the voltage range of 0.15–1.50 V at the scan rate of  $0.1 \text{ mV s}^{-1}$ . f) Reflectance spectra of representative colors at different voltage stages.

color periods and corresponding voltage ranges are quite stable, as shown in Figure S3d (Supporting Information).

The  $\text{Li}^+$  insertion/extraction reactions in the coloration films were investigated by cyclic voltammetry (CV). Figure 2e presents the CV profiles of the first three cycles of the coloration films. As can be seen, in the first cycle, there is a cathodic peak at around 0.50 V versus  $\text{Li}^+/\text{Li}$ , which indicates that the decomposition of electrolyte and the formation of a SEI layer happen in that voltage status.<sup>[31]</sup> Simultaneously, the color of films also starts to change from pristine orange-red to magenta at that time, which indicates the formation of a SEI layer on the film surface in the first cycle is related with this color change, causing from the irreversible minor thickness increase and the change of overall optical properties. It should be noted that two cathodic peaks at 0.40 V versus  $\text{Li}^+/\text{Li}$  and 0.23 V versus  $\text{Li}^+/\text{Li}$ , as well as two anodic peaks at 0.50 V versus  $\text{Li}^+/\text{Li}$  and 1.02 V versus  $\text{Li}^+/\text{Li}$ , are shown in all three cycles. The peaks and shape of the CV curve are consistent with the lithiation/delithiation mechanisms of a-Si anodes in lithium ion batteries (Figure S5, Supporting Information). The lithiation/delithiation reactions of  $\text{Li}^+$  with a-Si is believed to be



During the lithiation stage, the a-Si lattice is continuously broken up into Si clusters with the insertion of  $\text{Li}^+$ . The lithiation rate is highly depended on the a-Si lattice structure

integrity, the more and smaller Si clusters are broken up, the faster rate it has. At first, the lithiation rate is relatively slow because of the high resistance from integrated a-Si lattice structure. When the voltage continuously drops to around 0.40 V versus  $\text{Li}^+/\text{Li}$ , the first cathodic peak is observed at the CV curve, which is attributed to a start of faster insertion of  $\text{Li}^+$ . At this time, The Si lattice starts to break up into Si clusters much faster than before. It is also in accordance with the start of a faster volume increase of the a-Si thin film.<sup>[32,33]</sup> More importantly, comparing it with the chromatic process, the first cathodic peak at 0.40 V contributes to the color change in the chromatic stage, the faster  $\text{Li}^+$  insertion in the coloration films will cause the swell of the a-Si film and the change of its optical properties. When the voltage decreases to around 0.23 V versus  $\text{Li}^+/\text{Li}$ , another cathodic peak is shown in CV curve, by this point, a large number of small Si clusters have been formed, and further, these Si clusters start to break up into isolated Si atoms with the continuous insertion of  $\text{Li}^+$ . The lithiation rate is also faster than the former stage. The content of  $\text{Li}^+$  in  $\text{Li}_x\text{Si}$  film largely increases, causing the high effective refractive index and effective absorptivity of the overall coloration films, which provides a trigger function for the coloration films tuning from chromatic stage to achromic stage. During the delithiation stage, when the voltage increases from 0.15 to 0.5 V versus  $\text{Li}^+/\text{Li}$  (anodic peak), the isolated Si atoms grow back to larger Si clusters along with the extraction of  $\text{Li}^+$ . These Si nucleation sites will help to accelerate the formation of the final a-Si phase.

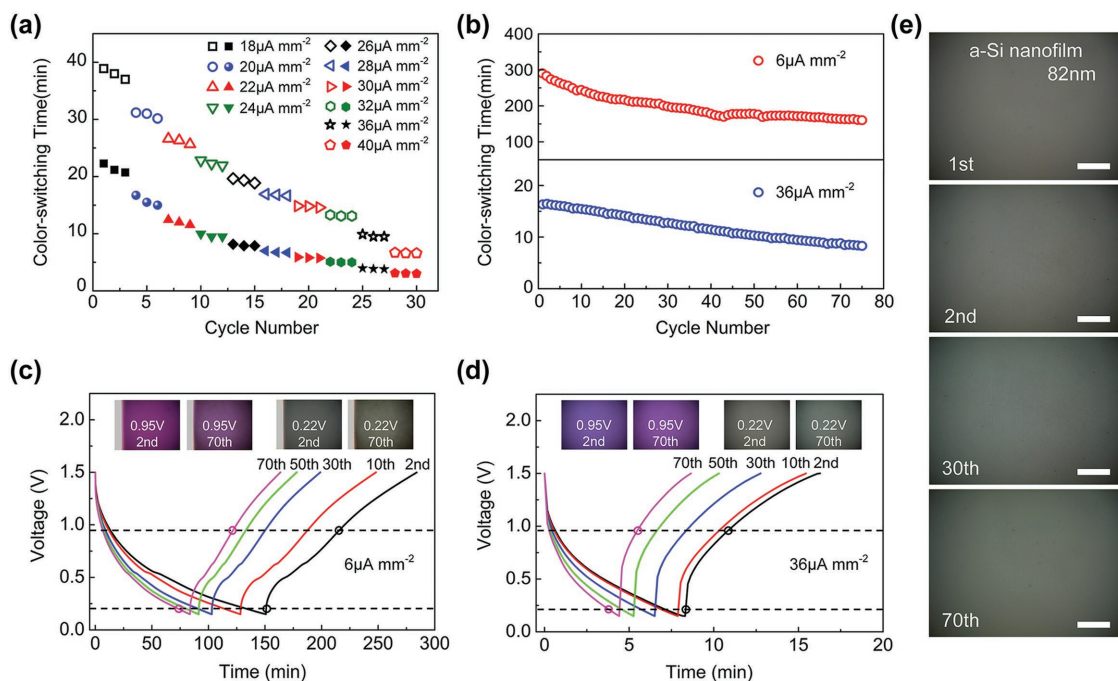
Simultaneously, the gray (achromic) color changes back to dark cyan, the function of thin film interference is rebooted. When the voltage increases to 1.02 V versus Li<sup>+</sup>/Li (anodic peak), the color stops to change gradually and returns to magenta. During this time, the amount of Li<sup>+</sup> in the Li<sub>x</sub>Si is very little; most of the Si clusters grow back to a-Si. It can be seen that similar relations between the coloration process and electrochemical reactions are found in both lithiation and delithiation stage, confirming the excellent reversibility of Li<sup>+</sup> extraction/insertion and color change in the as-prepared coloration films.

Figure 2f displays the reflectance spectra of different representative colors for interference coloration films, in the range of 400 to 700 nm. For pristine coloration film at a voltage of 1.50 V, a decrease of reflectance is observed when comparing the reflectance of the copper substrate. Note that a valley of reflectance is generated in the wavelength of 480 nm, which is ascribed to the addition of silicon layer above the copper substrate. During the lithiation stage, the position of the valley continuously shifts to long wavelength direction, and reaches to the wavelength of 600 nm at the voltage of 0.32 V. When voltage continues to drop, the curve of reflectance gradually tend to flat; this could be significant evidence that the coloration film could be reversibly switched to achromic by controlling the potential of the coloration film.

To investigate the color-switching time of the controllable coloration films, the corresponding coloration response under different current densities in the well-chosen voltage range of 0.22–1.40 V and 0.15–1.50 V was measured, as illustrated in Figure 3a and Figure S6 (Supporting Information). The color-switching time in this work is defined as the cycle period when

the color changes from magenta to gray (achromic), then return to magenta. It is noteworthy that the color-switching time contains the time when coloration film enters the achromic stage. As can be seen, the color-switching time is highly adjustable by the current density, which could be changed from hundreds of minutes to a few minutes. By carefully choose voltage range (0.22–1.40 V), the minimum color-switching time could decrease to around 3 min (190 s).

The stability and cycling performance of the coloration films is illustrated in Figure 3b. As the cycle goes on, the color-switching time is decreasing at the first few cycles and then tends to stable at around 150 and 8 min under current densities of 6 and 36 μA mm<sup>-2</sup>, respectively. Meanwhile, the coloration photographs at different cycle numbers combining with the charge/discharge curves are also shown in Figure 3c,d and Figure S7 (Supporting Information). On the one hand, even though the period of the cycle is decreasing, the profile of charge/discharge curves is changeless to some extent, which means that the electrochemical reaction is stable and in good agreement with CV results. On the other hand, the coloration photographs corresponding to the same voltages at second and 70th cycles show not only a well stability in chromatic properties of the coloration film but also the integrated uniform surface of a-Si layer without cracks and destruction. The stability of the coloration films could be attributed to the ultrathin silicon layer on the copper substrate and the proper voltage range in charge/discharge process.<sup>[34]</sup> Based on the coloration films fabrication, the thickness of the a-Si layer is smaller than the critical fracture size of a-Si, which is estimated to be about 300 nm.<sup>[35]</sup> Comparing to the thick silicon nanofilm (300 nm) on copper



**Figure 3.** The stability and cycling performance of the controllable coloration films. a) Color-switching time for the coloration films under different currents density in the potential range of 0.15–1.50 V (hollow) and 0.22–1.40 V (solid) ranging from 18 to 40 μA mm<sup>-2</sup>. b) Cycling performance of the coloration films under two current densities of 6 and 36 μA mm<sup>-2</sup> in the potential range of 0.15–1.50 V. c,d) Charge/discharge curves of the coloration films at different cycle period under two current densities of 6 μA m and 36 μA mm<sup>-2</sup>, respectively. e) The photograph of the robust surface of the silicon nanofilm (82 nm) during 70th cycles under current densities of 6 μA mm<sup>-2</sup>. The photographs are both captured at 0.22 V. The scale bar is 50 μm.

layer (Figure S8a,b, Supporting Information), the ultrathin a-Si film shows good structure robustness after 70 cycles in Figure 3e, while the thick silicon film appears several cracks and even the interfacial debonding only after four cycles. Meanwhile, the critical stress for cracking and plastic deformation is larger in the thin films than those in the thick films,<sup>[36]</sup> which means the thinner silicon film has superior ability to avoid the mechanical degradation during the Li<sup>+</sup> insertion and extraction process. Finally, the well-chosen coloration voltage range and stable thin film structure ensure that the film is incompletely

lithiated, which effectively reduces the stress value, the crack initiation, and materials fatigues in the film.

The electro-chemomechanical mechanism can be understood experimentally and theoretically as follows. The optical components of the controllable coloration films are obtained by the SE measurements (also see Supplementary methods in the Supporting Information). As shown in Figure 4a, the SE models and simulation equivalent models are established at both delithiated state and lithiated state. In the SE models, the a-Si layer is modeled as a Brendel oscillator, while the optical

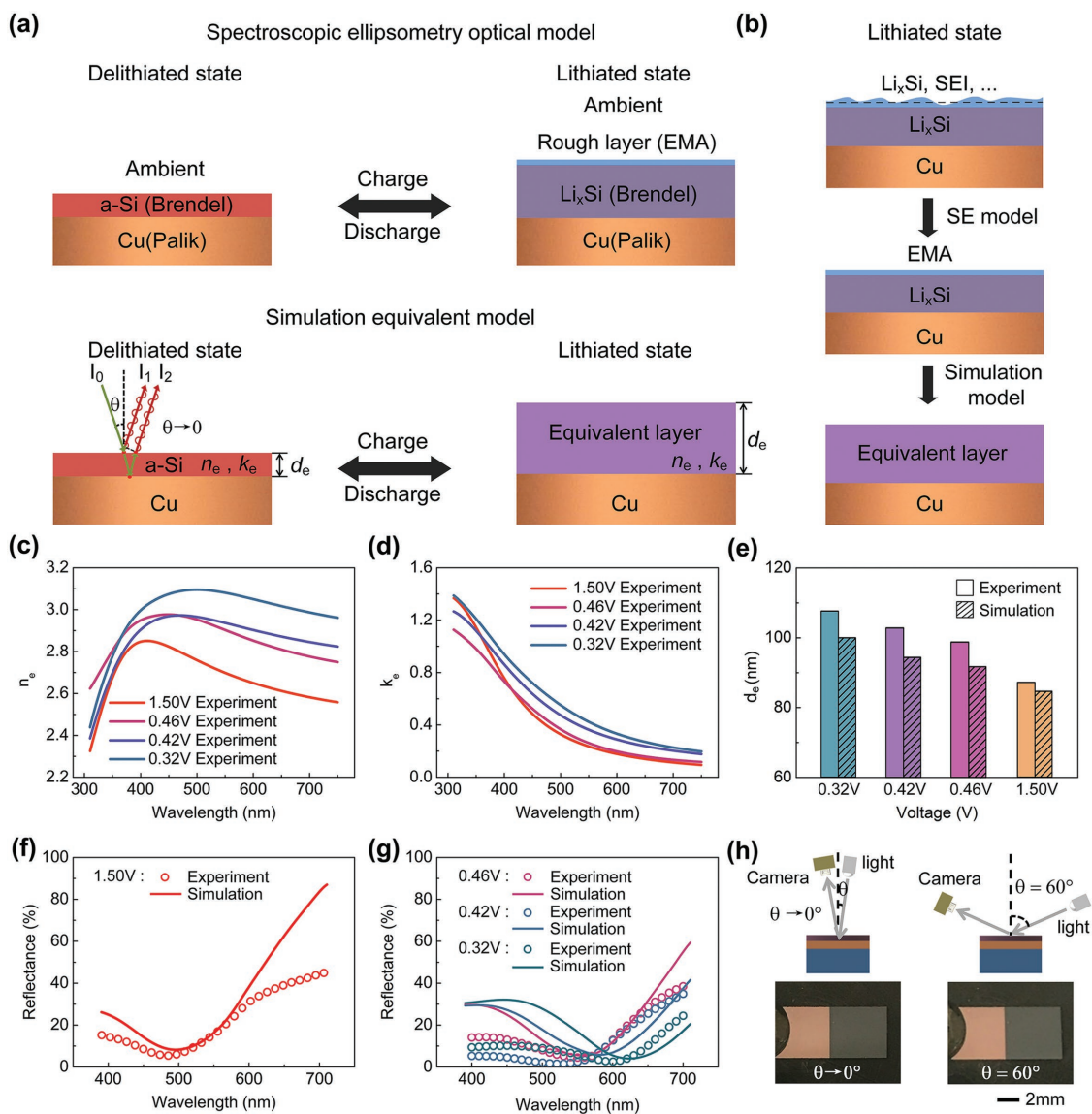


**Figure 4.** Electrochemical and mechanical mechanism in the controllable coloration films. a) The physical and simulation model used in the spectroscopic ellipsometry measurements and simulation reflectance fitting. b) The approximation approach of the silicon-based controllable coloration film after Li intercalation (from the original state to SE model and simulation model). Effective optical components of the layered structure, c) refractive index, and d) absorptivity, calculated from the spectroscopic ellipsometry results at different voltage stages. e) Bar graph indicates the chromatic layer (a-Si layer) thickness obtained from SE measurements and assumed in the simulation models at different voltage stages. The relative error range between SE experiment and simulation is controlled in 9%. Experiment and simulation reflectance results of the silicon-based controllable coloration film at f) 1.50 V, g) 0.46, 0.42, and 0.32 V voltage stages. h) The photographs of silicon-based controllable coloration film at 0.22 V discharge state shot from a different angle ( $0^\circ$  and  $60^\circ$ ).

constants of the copper substrate layer are found in the Palik optical handbook at delithiated state. For the lithiated state, the surface of coloration film is complicated in its components and has a rough ultrathin SEI layer,<sup>[37–39]</sup> as displayed in Figure 4b. To simplify the physical model, the effective medium approximation (EMA) layer is added up to the Li<sub>x</sub>Si layer (Brendel oscillator), and the a-Si layer is ignored because of the uniform Li intercalation in our experiments. The optical constants and the thickness of copper layer are not changed in both two states. Finally, the SE measurements were tested ex situ in the air ambient quickly to ensure the stability state of the film. In the simulation equivalent model, only two layers are considered in both delithiated and lithiated states (also see details at Supplementary methods in the Supporting Information). The equivalent layer is on the top of the copper layer, served as an enhancement reflection coating and metalized film respectively (Figure 4a). The reflectance intensity  $I_R$  of the layers could be given by the principle of superposition

$$I_R = I_1 + I_2 + 2\sqrt{I_1 I_2} \cos \varphi \quad (2)$$

where  $I_1$  is the intensity of reflected light on the surface of the equivalent layer;  $I_2$  is the intensity of the first emergent light on the surface of the equivalent layer;  $\varphi$  is the phase difference between the two interference lights, the above three variables can be written as follows

$$I_1 = I_0 \left( (n_e - 1)^2 + k_e^2 \right) / \left( (n_e + 1)^2 + k_e^2 \right) \quad (3)$$

$$I_2 = I_0 R_{Cu} (1 - R_e) e^{-8\pi k_e d_e / \lambda} \quad (4)$$

$$\varphi = 4\pi d_e n_e / \lambda + \pi \quad (5)$$

where  $R_e$  and  $R_{Cu}$  are the reflectances of the equivalent layer and copper layer, respectively,  $I_0$  is the intensity of incident light. Combining Equation (2) to Equation (5), the reflectance  $R$  of the entire structure could be a computable function as follows

$$R = I_R / I_0 = R(n_e(\lambda), k_e(\lambda), d_e, R_{Cu}(\lambda)) \quad (6)$$

where  $\lambda$  is the light wavelength in a vacuum. There are three types of control parameters in the chromatic process. The first is optical components of the equivalent layer including effective refractive index,  $n_e(\lambda)$ , and effective absorptivity,  $k_e(\lambda)$  in the visible wavelength, which could be respectively calculated by using a thickness-weighted average of optical components for a-Si layer (delithiated state) or EMA and Li<sub>x</sub>Si layer (lithiated state) derived from SE measurements. Effective refractive index and effective absorptivity at the delithiated state and three lithiated states (0.46, 0.42, and 0.32 V corresponding to Figure 2f) are shown in the Figure 4c,d, respectively. There is an increase of the effective refractive index above 450 nm upon lithiation, while the effective absorptivity increases slightly upon lithiation. This slight change of two optical parameters will only make a fraction of contribution to variation in the reflectance spectrum of the entire films. On the other hand, the second

type control parameter, the equivalent layer thickness,  $d_e$  plays a major contribution to the color change of the films. As shown in Figure 4e, the thickness of the equivalent layer increases with the Li-ion insertion during the discharge process,<sup>[40]</sup> causing the variable destructive interference at different lithiated state. The third is the reflectance of the substrate layer, when substrate layer is determined (e.g., copper), it can be tested by the spectrometer (Figure 2d), and  $R_{Cu}(\lambda)$  is invariable during the simulation. To verify the rationality of our simulation model, the simulated reflectance at delithiated state (1.5 V, pristine) is derived, which closely resembles the corresponding experimental data, especially at the valley of the curves (Figure 4f). Moreover, the relative error of thickness between the SE results and simulation is only 2.3%. The deviation of the two curves below the 450 nm and above the 600 nm is mainly caused by the difference of incident light intensity between the experiment and ideal simulation. Furthermore, as the comparison between experimental data and simulation at different lithiated states is shown in Figure 4g, the shift of the valley to the long wavelength is consistent in both experimental data and simulation. It should note that this valley shift in the reflectance spectrum determines the corresponding color change of the films. In the simulation equivalent models, these three types of control parameters coordinate the variation of reflectance of entire films. The parameter analysis shows that when the reflectance of the substrate layer,  $R_{Cu}(\lambda)$  is constant, the change of optical components ( $n_e$  and  $k_e$ ) contributes little to the change of the reflectance spectrum, while the change of the equivalent layer thickness makes the major contribution to the valley shift in the reflectance spectrum (Figure 4g). Consequently, in the chromatic state, the swell/shrinkage of the equivalent layer corresponding to the thickness change plays a leading role in the color tuning, while the optical components change plays assistance. On the contrary, when the film is under achromic state, the high absorption of the equivalent layer weakens the destructive interference effects. And the whole film shows the uniform reflectance spectrum which is the color of the equivalent layer. To prove that, a simple observation experiment is showed in Figure 4h and Figure S9 (Supporting Information). The gray (achromic) film at 0.22 V (lithiated state) is observed vertically from the top view and with an angle of 60°. As is known, the destructive interference effect is influenced by the light incident angle and observation angle. But the color recorded by charge coupled device (CCD) camera is nearly unchanged, which means that the gray is the color of the equivalent layer without the effects of destructive interference. Besides, the angle influence of destructive interference for observed films in variable chromatic state is also demonstrated in Figure S9 (Supporting Information). The dark blue film can be changed to medium purple clearly when the observation angle turn to 85°, while the gray is unchanged at that angle.

To demonstrate the designability of the controllable coloration films, three different kinds of films, with 82 and 63 nm a-Si layer on the copper substrate, and 77 nm a-Si layer on the silver substrate, were readily fabricated by changing the thickness of initial a-Si layer and the types of the reflective metal substrate as illustrated in Figure 5a. The initial thickness of three different coloration films is tested by a profilometer, as

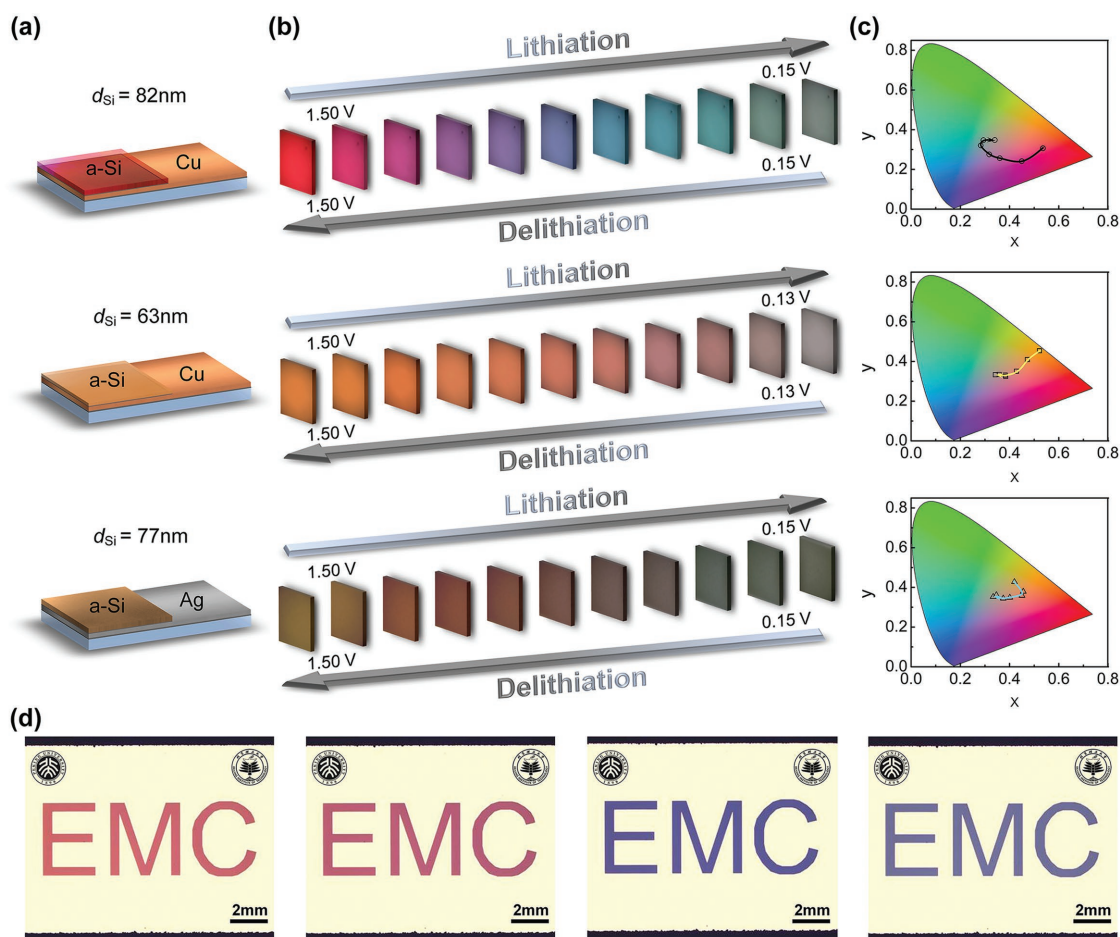


**Figure 5.** Demonstration of the silicon-based controllable coloration films designability. Structural a) schematic and b) the corresponding chromatic performance of silicon-based controllable coloration film with 82 and 63 nm a-Si layers on the copper current collector, and silicon-based controllable coloration film with 77 nm a-Si layer on the silver current collector. The photographs in (b) are shot from the top of the view. c) The color evolution of three kinds of silicon-based controllable coloration film in the CIE chromaticity charts. (black solid: 82 nm a-Si, copper substrate; yellow solid: 63 nm a-Si, copper substrate; blue solid: 77 nm a-Si, silver substrate). d) The chromatic patterned silicon-based controllable coloration film (82 nm a-Si, copper substrate) under the control of voltage.

shown in Figure S10 (Supporting Information). Comparisons of three different films in chromatic performance are shown in Figure 5b. According to the CIE 1931 standard color-matching functions, the color evolution of three different films is also demonstrated in the CIE chromaticity chart in Figure 5c. They show the different color at the chromatic stage, while all of them enter into the achromic part under the voltage control. It should be noted that this reversible voltage control chromatic performance shows the feasibility in the camouflage technology, anticounterfeiting and the sensor technology for monitoring the state of silicon-based energy devices. Moreover, using the shadow mask technique, the coloration films can also be easily patterned into variable shapes. As shown in Figure 5d and Figure S11 (Supporting Information), the designed chromogenic device with patterned coloration films exhibits a stable and uniform color change process.

The results of the optical and electrochemical experiments along with theoretical modeling imply that the electro-chemo-mechanical chromic phenomenon is a fundamental structural effect from the assembled optical reflection structure based on

silicon nanofilms and metal substrates. Reversible lithiated/delithiated a-Si film plays a critical role in manipulating the destructive interference for achieving consecutively controllable coloration in a broad visible band with the switch capability from chromatic to achromic state. Because of uniform volumetric expansion and shrinkage in the a-Si nanoscaled films, such alloyable films would be more likely to be a bifunctional optical filter, and thus both structural destructive interference and material optical parameters could be simultaneously altered. Whereby, a series of devices are available via simply changing the initial conditions of the coloration films. As the thickness of a-Si nanofilms and the original color of reflective metal substrate are varied, the corresponding destructive interference condition and intrinsic absorbed coloration would be completely changed in the coloration films (Figure 5).

In the perspectives for versatility and applications, the mechanism of coloration demonstrated in the present coloration films allows for designing various smart multiple-coloration devices with simple materials, and the essential variable nanofilms could be extended from silicon anodes to tin (Sn), germanium

(Ge), and related alloying anodes that could be reversibly lithiation/delithiated. As a result, the visible band with controllable coloration would be substantially broadened. For the configuration of lithium ion batteries, more importantly, such devices could be modified into energy storage devices via updating with cathode materials, and whereby a multifunction lithium ion battery would be envisaged. Additionally, the lithiation/delithiation rate and color-switching rate will be further improved by optimizing the density and the microstructural design of a-Si layer. Hence, the bioinspired controllable coloration films would hold great opportunities in smart optical devices with reflective configuration, and therefore specular reflection, sensing, anticounterfeiting, labels, displaying, and sensors are expected to be promoted.

### 3. Conclusions

In summary, novel types of controllable coloration films have been developed based on silicon nanoscaled films and metal substrates. The as-fabricated coloration films present superior reflectance selectivity and distinctive switch capability between the chromatic and achromic reflectance. Collection of both experimental and theoretical studies has well described the fundamental electro-chemomechanical coloration mechanisms. The controllable coloration films exhibit a wide color change range, stable cycle performance, and unique reflective intensity tunability. Such bioinspired interference coloration design would potentially provide a new active control modulation for achieving color diversity in a broad wavelength range.

### 4. Experimental Section

**Preparation of the Controllable Coloration Films:** The controllable coloration film was obtained by RF magnetron sputtering using a KJLC LAB18 Film Deposition System. Four thin layers of chromium (Cr, 10 nm), copper (Cu, 100 nm), Cr (5 nm), and then amorphous silicon (a-Si, 82 nm) were deposited in sequence on the glass wafer (4 in.). The Cr/Si (5 nm/82 nm thick) layers were patterned in a working pressure of 3 mTorr using a shadow mask technique. The power used for Cr/Si sputtering was 65 W. The thickness of the amorphous silicon layer and the copper layer was verified by a profilometer (Dektak XT). Then, the sputtered wafer was diced into a rectangular film (5 mm × 10 mm) for the convenience of electrochemical testing.

**Electrochemical Measurements:** The electrochemical performance was evaluated at a home-made electrochemical reaction device, which was configured by using the prepared electrochromic film as the anode with lithium metal foil as reference and counter electrode (Alfa Aesar). The electrolyte was 1 M LiPF<sub>6</sub> dissolved in 1:1 (v/v) DMC:EC (Fosai New Material Co. Ltd.). All assembly manipulations were carried out in a glove box (Mbraun Inc.) filled with high-purity argon. Galvanostatic charge/discharge properties of the film were investigated in the potential range from 0.15 to 1.50 V and from 0.22 to 1.40 V (vs Li/Li<sup>+</sup>) at 298 K by a BT-2000 battery testing system (Arbin USA). The CV was measured using the Bio-Logic VMP3 electrochemical workstation in the voltage range of 0.15–1.50 V (versus Li/Li<sup>+</sup>) at the scan rate of 0.1 mV s<sup>-1</sup>.

**Optical Measurements:** For in situ optical observation, an optical microscope (Keyence Corporation) was used while galvanostatic current density was applied to the electrochromic coloration films (Figure S1, Supporting Information). An ex situ optical transmission system based on a fiber optic spectrometer (Avantes AvaSpec-ULS2048) combined with an optical microscope (Zeiss Axio Scope.A1) was used to acquire the reflectance of the electrochromic film, which was disassembled from

the reaction cell inside the glove box and washed by dimethyl carbonate (DMC) subsequently. Spectroscopic ellipsometry (SE) measurements were taken from 200 to 900 nm at an angle of 70° by means of a spectroscopic ellipsometer (SENTECH SE 850 DUUV). The instrumental software was used to perform the fitting of  $\Psi$  and  $\Delta$ . All the ex situ tests were carried out in a short time to ensure the accuracy of the experimental data.

**Quantitative Connection between Colors and Voltage:** A series of recorded photographs was digitized by MATLAB R2014a. The average HSL color values (hue, saturation, lightness) of each photograph were obtained by the self-compiled code. The gray (achromic) state of the coloration film was first defined by the range of saturation from 0 to 0.1. The four representative colors at chromatic state were strictly divided according to the standard hue division from Munsell color system (also see details at Supplementary methods in the Supporting Information). The related voltage ranges of representative colors and the switch points were further determined by the corresponding color division.

**Theoretical Model Calculation:** To calculate the reflectance of controllable coloration film, mathematical analysis software, MATLAB R2014a was used to calculate the theoretical reflective intensity of the layered structures with the input data of effective refractive index,  $n_e(\lambda)$ , and effective absorptivity,  $k_e(\lambda)$ , and the reflectance of the copper layer,  $R_{Cu}(\lambda)$ , in each wavelength from 400 to 700 nm. The rationality of the model can be verified by comparing the equivalent layer thicknesses measured by SE tests with the assumed thicknesses in models.

### Supporting Information

Supporting Information is available from the Wiley Online Library or from the author.

### Acknowledgements

Y.B. and Y.H. contributed equally to this work. The authors appreciated the fruitful discussion and support from Prof. Hai-Zheng Zhong at Beijing Institute of Technology. The authors gratefully acknowledge the financial support by the National Natural Science Foundation of China (No.11672341 and No.11572002) and National Basic Research Program of China (No. 2015CB932500); Supports by the Innovative Research Groups of the National Natural Science Foundation of China (No. 11521202), the National Materials Genome Project (No. 2016YFB0700600) and Beijing Natural Science Foundation (No. 16L00001) are also acknowledged. Y.B. acknowledges financial support from China Scholarship Council.

### Conflict of Interest

The authors declare no conflict of interest.

### Keywords

bioinspired materials, consecutive broadband, interference colors, silicon electrodes, smart films

Received: September 9, 2018

Revised: October 20, 2018

Published online:

- [1] R. M. Kramer, W. J. Crookes-Goodson, R. R. Naik, *Nat. Mater.* **2007**, *6*, 533.
- [2] K. M. Cooper, R. T. Hanlon, B. U. Budelmann, *Cell Tissue Res.* **1990**, *259*, 15.

- [3] M. Rassart, P. Simonis, A. Bay, O. Deparis, J. P. Vigneron, *Phys. Rev. E* **2009**, *80*, 31910.
- [4] J. P. Vigneron, J. M. Pasteels, D. M. Windsor, Z. Vértesy, M. Rassart, T. Seldrum, J. Dumont, O. Deparis, V. Lousse, L. P. Biró, *Phys. Rev. E* **2007**, *76*, 31907.
- [5] C. Yu, Y. Li, X. Zhang, X. Huang, V. Malyarchuk, S. Wang, Y. Shi, L. Gao, Y. Su, Y. Zhang, H. Xu, R. T. Hanlon, Y. Huang, J. A. Rogers, *Proc. Natl. Acad. Sci. USA* **2014**, *111*, 12998.
- [6] S. Hirata, T. Tsuji, Y. Kato, C. Adachi, *Adv. Funct. Mater.* **2012**, *22*, 4195.
- [7] Z. Zhang, K. Guo, Y. Li, X. Li, G. Guan, H. Li, Y. Luo, F. Zhao, Q. Zhang, B. Wei, *Nat. Photonics* **2015**, *9*, 233.
- [8] M. Qin, M. Sun, R. Bai, Y. Mao, X. Qian, D. Sikka, Y. Zhao, H. J. Qi, Z. Suo, X. He, *Adv. Mater.* **2018**, *30*, 1800468.
- [9] J. Zhang, S. He, L. Liu, G. Guan, X. Lu, X. Sun, H. Peng, *J. Mater. Chem. C* **2016**, *4*, 2127.
- [10] G. Huang, Y. Yin, Z. Pan, M. Chen, L. Zhang, Y. Liu, Y. Zhang, J. Gao, *Biomacromolecules* **2014**, *15*, 4396.
- [11] Y. Zhao, Z. Xie, H. Gu, C. Zhu, Z. Gu, *Chem. Soc. Rev.* **2012**, *41*, 3297.
- [12] A. V. Yakovlev, V. A. Milichko, V. V. Vinogradov, A. V. Vinogradov, *ACS Nano* **2016**, *10*, 3078.
- [13] L. Phan, D. D. Ordinario, E. Karshalev, W. G. Walkup IV, M. A. Shenk, A. A. Gorodetsky, *J. Mater. Chem. C* **2015**, *3*, 6493.
- [14] K. Watanabe, T. Hoshino, K. Kanda, Y. Haruyama, S. Matsui, *Jpn. J. Appl. Phys.* **2005**, *44*, L48.
- [15] Z. Song, C. Lv, M. Liang, V. Sanphuang, K. Wu, B. Chen, Z. Zhao, J. Bai, X. Wang, J. L. Volakis, L. Wang, X. He, Y. Yao, S. Tongay, H. Jiang, *Small* **2016**, *12*, 5401.
- [16] J. Zhu, Z. Yu, G. F. Burkhard, C. Hsu, S. T. Connor, Y. Xu, Q. Wang, M. McGehee, S. Fan, Y. Cui, *Nano Lett.* **2009**, *9*, 279.
- [17] Y. Huang, S. Chattopadhyay, Y. Jen, C. Peng, T. Liu, Y. Hsu, C. Pan, H. Lo, C. Hsu, Y. Chang, *Nat. Nanotechnol.* **2007**, *2*, 770.
- [18] Q. Wang, G. R. Gossweiler, S. L. Craig, X. Zhao, *Nat. Commun.* **2014**, *5*, 4899.
- [19] X. Gao, X. Yan, X. Yao, L. Xu, K. Zhang, J. Zhang, B. Yang, L. Jiang, *Adv. Mater.* **2007**, *19*, 2213.
- [20] H. Li, X. Sun, H. Peng, *ChemPhysChem* **2015**, *16*, 3761.
- [21] Y. Kang, J. J. Walsh, T. Gorishnyy, E. L. Thomas, *Nat. Mater.* **2007**, *6*, 957.
- [22] M. Xiao, Y. Li, J. Zhao, Z. Wang, M. Gao, N. C. Gianneschi, A. Dhinojwala, M. D. Shawkey, *Chem. Mater.* **2016**, *28*, 5516.
- [23] X. Sun, J. Zhang, X. Lu, X. Fang, H. Peng, *Angew. Chem., Int. Ed.* **2015**, *54*, 3630.
- [24] E. P. Chan, J. J. Walsh, E. L. Thomas, C. M. Stafford, *Adv. Mater.* **2011**, *23*, 4702.
- [25] C. G. Schäfer, M. Gallei, J. T. Zahn, J. Engelhardt, G. P. Hellmann, M. Rehahn, *Chem. Mater.* **2013**, *25*, 2309.
- [26] J. Lang, B. Ding, T. Zhu, H. Su, H. Luo, L. Qi, K. Liu, K. Wang, N. Hussain, C. Zhao, X. Li, H. Gao, H. Wu, *Adv. Mater.* **2016**, *28*, 10236.
- [27] Y. An, B. C. Wood, J. Ye, Y. Chiang, Y. M. Wang, M. Tang, H. Jiang, *Phys. Chem. Chem. Phys.* **2015**, *17*, 17718.
- [28] C. Yu, X. Li, T. Ma, J. Rong, R. Zhang, J. Shaffer, Y. An, Q. Liu, B. Wei, H. Jiang, *Adv. Energy Mater.* **2012**, *2*, 68.
- [29] X. Zhang, W. Song, Z. Liu, H. Chen, T. Li, Y. Wei, D. Fang, *J. Mater. Chem. A* **2017**, *5*, 12793.
- [30] S. P. V. Nadimpalli, V. A. Sethuraman, S. Dalavi, B. Lucht, M. J. Chon, V. B. Shenoy, P. R. Guduru, *J. Power Sources* **2012**, *215*, 145.
- [31] L. B. Chen, J. Y. Xie, H. C. Yu, T. H. Wang, *J. Appl. Electrochem.* **2009**, *39*, 1157.
- [32] B. Key, M. Morcrette, J. Tarascon, C. P. Grey, *J. Am. Chem. Soc.* **2011**, *133*, 503.
- [33] L. Y. Beaulieu, T. D. Hatchard, A. Bonakdarpour, M. D. Fleischauer, J. R. Dahn, *J. Electrochem. Soc.* **2003**, *150*, A1457.
- [34] S. K. Soni, B. W. Sheldon, X. Xiao, A. F. Bower, M. W. Verbrugge, *J. Electrochem. Soc.* **2012**, *159*, A1520.
- [35] J. Graetz, C. C. Ahn, R. Yazami, B. Fultz, *Electrochem. Solid-State Lett.* **2003**, *6*, A194.
- [36] H. Haftbaradaran, X. Xiao, H. Gao, *Modell. Simul. Mater. Sci. Eng.* **2013**, *21*, 074008.
- [37] J. Duay, K. W. Schroder, S. Murugesan, K. J. Stevenson, *ACS Appl. Mater. Interfaces* **2016**, *8*, 17642.
- [38] M. Gauthier, T. J. Carney, A. Grimaud, L. Giordano, N. Pour, H. Chang, D. P. Fenning, S. F. Lux, O. Paschos, C. Bauer, *J. Phys. Chem. Lett.* **2015**, *6*, 4653.
- [39] C. K. Chan, R. Ruffo, S. S. Hong, Y. Cui, *J. Power Sources* **2009**, *189*, 1132.
- [40] G. Bucci, S. P. V. Nadimpalli, V. A. Sethuraman, A. F. Bower, P. R. Guduru, *J. Mech. Phys. Solids* **2014**, *62*, 276.